Applied Acoustics 211 (2023) 109459

Contents lists available at ScienceDirect

Applied Acoustics

journal homepage: www.elsevier.com/locate/apacoust

Investigation of the mechanism of noise radiation reduction from an ABH-cavity under interior acoustic excitation considering multistage coupling

Hanfeng Ye [a], Hongli Ji [a,*], Chaoyan Wang [a,b], Chongcong Tao [a], Li Cheng [c], Jinhao Qiu [a]

[a] State Key Laboratory of Mechanics and Control of Mechanical Structures, Nanjing University of Aeronautics and Astronautics, Nanjing, China
[b] Nanjing Institute of Information Technology, Nanjing, China
[c] Department of Mechanical Engineering, Hong Kong Polytechnic University, Hung Hom, Kowloon, Hong Kong

ARTICLE INFO

Article history:
Received 17 March 2023
Received in revised form 22 May 2023
Accepted 23 May 2023

Keywords:
Acoustic black hole
Noise radiation reduction
Plate-cavity
Coupling analysis

ABSTRACT

The acoustic black hole (ABH) structure exhibits superior vibration and sound radiation control capability compared to its flat counterpart. However, for a coupled plate-cavity system under interior acoustic excitation, the underlying suppression mechanism of noise radiation has not been explored, especially below the critical frequency of the structure. In this paper, the noise suppression mechanism of an ABH-cavity system under interior acoustic excitation is investigated both theoretically and numerically. Based on the theoretical analysis, the noise radiation depends on both the structural modes and the cavity modes, which can be suppressed in two ways. One is to lower the magnitude of structural transfer functions. The other is to change the mapping matrix which maps the structural modal amplitude to the amplitude of radiation modes. For the former, numerical analysis based on FEM demonstrates that a lower structural transfer function is obtained in the ABH-cavity system compared to its flat counterpart because of the damping enhancement characteristic of the ABH structure. Therefore, attenuated flexural vibrations and reduced sound radiation are achieved at corresponding modal frequencies. For the latter, ABH-cavity systems with varying numbers of ABHs are constructed to demonstrate a simple solution of manipulating the mapping matrix to achieve the reduced radiation efficiency of structural panels and the enhanced suppressing effect of noise radiation. The study in this paper indicates a feasible direction for the further optimization analysis of noise radiation suppression of the ABH-cavity system.

1. Introduction

The problem of noise radiation [1,2] (or the break-out noise) of a coupling system between acoustic space and flexible structure is very common and important in heating, ventilation and air conditioning (HVAC) ducts, aircraft cabins, space capsules, etc. Many studies about the noise radiation of the structural–acoustic coupling system focus on the numerical modeling [3–5], investigations on the effects of different geometrical forms [5,6], analytical models of prediction [7–9] and the noise suppression of active noise control [10]. Compared with active control, passive control is always a reliable and economic option in applications. A representative technique of the traditional passive control is using extensive damping material for vibration control [11]. However, these extra dissipative components inevitably increase the mass of the whole system considerably.

Recently, there has been growing interest in utilizing acoustic black hole (ABH) structures for efficient passive structural vibration control [12]. The concept of ABH was first introduced by Mironov in 1988 [13]. ABH structures exhibit the phenomenon of energy localization and damping dissipation [14], which is a result of trapped flexural waves in the ABH region due to local heterogeneities in stiffness or damping. This enhanced damping capability has led to the application of ABHs in numerous numerical and experimental analyses for vibration control. Various analytical methods have been employed to study the damping mechanism of ABHs. These include the geometric acoustic approach [15,16] and the impedance method [17]. For handling complex boundary problems and multi-field coupling problems, the semi-analytical method [16,18–20] and the finite element method (FEM) [21–24] have been adopted. In experimental analyses of vibration control, ABH beams have been used to achieve low-frequency elastic wave

* Corresponding author.
E-mail address: jihongli@nuaa.edu.cn (H. Ji).

https://doi.org/10.1016/j.apacoust.2023.109459
0003-682X/

Nomenclature

A_e	area of each element in coupling interface S [m^2]
$\boldsymbol{B}$	a vector related to nodal load [m]
$\boldsymbol{C}$	damping matrix [kg/s]
E	Young's modulus [Pa]
$\boldsymbol{F}$	excitation force [N]
I	sound intensity [W/m^2]
$\boldsymbol{K}$	stiffness matrix [N/m]
L	the total number of the radiation mode [dimensionless]
$\boldsymbol{M}$	mass matrix [kg]
N	the total number of the elements [dimensionless]
$\boldsymbol{P}$	spatial distribution matrix of radiation modes [dimensionless]
$\boldsymbol{R}$	radiation resistance matrix [kg/s]
S; S'	integration surface [m^2]
$\boldsymbol{T}$; T_{si}; T_{aj}	matrix of transfer functions; the transfer function of the i^{th} structural mode; the transfer function of the j^{th} cavity mode [$rad^{-2}*s^2$]
V	interior domain of the cavity [m^3]
W	sound power [W]
$\boldsymbol{Z}$	impedance matrix [$kg*m^{-2}*s^{-1}$]
a	a constant of power-law profile of the ABH part [dimensionless]
c_0	velocity of sound in air [m/s]
d_{ij}	distance between the centers of the i^{th} and j^{th} elements in the coupling interface [m]
f	frequency [Hz]
h; h_0	thickness; residual thickness [m]
i	the order of the structural mode (i = 1,2,...,m) [dimensionless]
j	the order of the cavity mode (j = 1,2,...,n) [dimensionless]
j	imaginary unit [dimensionless]
k'	wavenumber [m^{-1}]
l	the order of the radiation mode (l = 1,2,...,L) [dimensionless]
m	the total number of the structural mode [dimensionless]
n	the total number of the cavity mode [dimensionless]
$\boldsymbol{p}$; p	vector of sound pressure; sound pressure [Pa]
q	amplitude of the monopole sound source [kg/s^2]
r; r_0; r_1	radius; the radius of the central platform; the radius of the whole ABH area [m]
u	acoustic particle velocity [m/s]
$\boldsymbol{v}$; v	vector of structural velocity; structural velocity [m/s]
$\boldsymbol{w}$; w	structural displacement [m]
x_l	eigenvalues of diagonal matrix $\boldsymbol{\Lambda}$ [kg/s]
$\boldsymbol{y}$; y_l	vector of radiation modes in terms of velocities of the individual radiators; the l^{th} radiation modes in terms of velocities of the individual radiators [m/s]

Greek symbols

$\boldsymbol{\Lambda}$	diagonal matrix of eigenvalues x_i [kg/s]
$\boldsymbol{\Phi}$;ϕ_i	structural modal shape functions; the i^{th} structural modal shape [dimensionless]
$\boldsymbol{\Psi}$; ψ_j	pressure distribution functions of cavity modes; the j^{th} pressure distribution [dimensionless]
φ	spatial distribution vector of radiation modes [dimensionless]
$\boldsymbol{\Theta}$	a matrix that transforms the nodal displacement vector to normal surface displacement vector [dimensionless]
Ω_p	surface set as Dirichlet boundary condition [dimensionless]
Ω_∞	boundary surface located at infinity [dimensionless]
Ω_v	surface set as rigid boundary condition [dimensionless]
Ω_s	radiation surface of the flexible panel [dimensionless]
Ω_z	surface set as Robin boundary condition [dimensionless]
ζ; ζ_{si}; ζ_{aj}	modal damping ratio; the i^{th} structural modal damping ratio; the j^{th} cavity modal damping ratio [dimensionless]
η	loss factor [dimensionless]
$\boldsymbol{\lambda}$; λ_{si}; λ_{aj}	vector of modal coordinates; the i^{th} structural modal coordinates; the j^{th} cavity modal coordinates [dimensionless]
μ	Poisson's ratio [dimensionless]
ρ; ρ_0	density; density of air [kg/m^3]
σ; σ'	radiation efficiency of the whole panels; self-radiation efficiency that represents the radiation efficiency of radiation modes [dimensionless]
ω; ω_{si}; ω_{aj}	angular frequency; the i^{th} structural modal frequency; the j^{th} cavity modal frequency [rad/s]

Subscripts and superscripts

AL	aluminum
H	Hermitian matrix
T	transpose of a matrix
a	acoustic
c	coupling
crit	critical
d	damping layer
n	normal direction
k	the serial number of N elements
ref	reference
s	structural
*	complex conjugate

attenuation [25]. The bandwidth of flexural and longitudinal waves in ABH beams can be adjusted by employing embedded mass oscillators [26]. In situations where structural space and design constraints arise, spiral ABHs [27,28] and vibration absorbers based on the ABH effect [29,30] can be attached to the host structure to control its vibrations.

While previous works have primarily focused on vibration control of ABHs, there has been a growing interest in studying the sound properties of ABH structures subjected to force excitation. Ma et al. [31,32] investigated the sound radiation of ABH plates under force excitation and found that these plates exhibit significantly reduced sound radiation efficiency across a wide dynamic frequency range compared to their uniform counterparts. Similarly, Deng et al. [33] demonstrated the effectiveness of annular ABHs in reducing air-borne radiation in free field conditions. Additionally, Tang et al. [34] examined the sound radiation properties of plates composed of periodically tangled ABH cells.

In the context of a more complex vibro-acoustic system, Feurtado and Conlon [35] demonstrated that ABHs redistribute supersonic vibrations into subsonic components, resulting in a reduction in sound radiation efficiency through wavenumber transfer analysis when the structure is subjected to a point force excitation. Additionally, Deng et al. [36] illustrated that ABHs are not only capable of reducing radiation in air cavities but also help suppress radiation in water [37]. Our previous numerical and experimental analyses [23,38] have also revealed a reduction in the coupling strength between the ABH plate and the cavity.

The aforementioned works have primarily focused on investigating the sound properties of ABH structures under force excitation. However, in practical applications, acoustic excitation is commonly encountered. In terms of sound transmission loss, several experiments [39,40] have demonstrated that ABH plates with a damping layer exhibit promising performance for transmission loss applications. Furthermore, concerning sound insulation between two cavities, with one of them being the sound source cavity, ABH plates have shown a significant improvement in transmission loss near the critical frequency of uniform plates, as analyzed through statistical modal energy distribution analysis (SmEdA) [41]. Although SmEdA is effective in estimating the average behavior of a population and is commonly used for efficient modeling at high frequencies, the prediction of detailed vibro-acoustic behavior of a specific sample at such frequencies still remains a challenge. Therefore, the comprehensive exploration of the underlying mechanism of a plate-cavity system under interior acoustic excitation, especially below the critical frequency (also known as coincident frequency), remains an area that requires further investigation.

As mentioned, ABH structures under a force excitation exhibit an excellent performance on the vibration and sound radiation control. Unlike the situation of the force excitation where the structural mode is the dominant factor to be considered, the cavity mode would have a significant influence on the noise radiation for a plate-cavity system under interior acoustic excitation. In this study, we aim to explore the underlying mechanism behind the suppression of radiated sound in the coupled ABH-cavity system through theoretical analysis and numerical verification using the finite element method (FEM). Our focus is primarily on frequencies below 2500 Hz (below the critical frequency where main noise reduction challenges remain), which are typically considered relevant for human auditory perception. It is important to note that the results obtained using FEM at lower frequencies are sufficient to demonstrate the relevant mechanisms. The insights gained from this study regarding the coupling mechanics between ABH structures and cavities can contribute to an enhanced understanding of the ABH effect and provide valuable guidance for the acoustic applications of ABH structures.

This paper is organized as follows. The theories of vibration and sound radiation of the coupled plate-cavity system are introduced, and the related suppression mechanisms of noise radiation are proposed in section 2. The FE models under investigation and the corresponding discussions are presented in section 3. In section 4, theoretical analyses of suppression mechanisms are verified by numerical studies of different plates with varying numbers of ABHs. Conclusions are drawn in section 5.

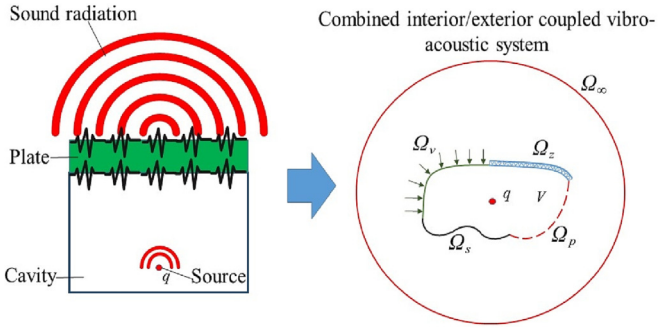

Fig. 1. Model of sound radiation of plate-cavity system excited under a monopole sound source. Ω_p for Dirichlet BC; Ω_z for Robin BC or mixed BC.

2. Theory

A schematic of the noise radiation of the cavity-plate system is shown in Fig. 1. A harmonic monopole sound source is placed in the rectangular cavity. The plate is excited by an acoustic excitation. The sound power radiated from the plate is examined. This process can be numerically regarded as a combined interior/exterior coupled vibro-acoustic problem. For the exterior domain of the far-field, the Sommerfeld radiation condition must be satisfied at the boundary surface Ω_∞. For the interior domain V of the cavity, all surfaces can be divided into three types of boundary condition (BC) [42]. This work focuses on the Neuman or natural boundary condition on the surface Ω_v (set as the rigid boundary for this case) and the surface Ω_s (set as the radiation surface of the flexible panel). For the completeness of the paper, previously developed theories about vibro-acoustic coupling system and sound radiation are briefly recalled as follows.

2.1. Vibration theory of the plate-cavity system

Note that the fluid loading caused by far-field is irrespective, the discretized interior vibro-acoustic coupling equation of the plate-cavity system can be expressed as [42]

$$\left(\begin{bmatrix} \boldsymbol{K}_\mathrm{s} & \boldsymbol{K}_\mathrm{c} \\ 0 & \boldsymbol{K}_\mathrm{a} \end{bmatrix} + \mathrm{j}\omega \begin{bmatrix} \boldsymbol{C}_\mathrm{s} & 0 \\ 0 & \boldsymbol{C}_\mathrm{a} \end{bmatrix} - \omega^2 \begin{bmatrix} \boldsymbol{M}_\mathrm{s} & 0 \\ \boldsymbol{M}_\mathrm{c} & \boldsymbol{M}_\mathrm{a} \end{bmatrix}\right) \cdot \begin{Bmatrix} \tilde{\boldsymbol{w}} \\ \tilde{\boldsymbol{p}} \end{Bmatrix} = \begin{Bmatrix} \tilde{\boldsymbol{F}}_\mathrm{s} \\ \tilde{\boldsymbol{F}}_\mathrm{a} \end{Bmatrix} \tag{1}$$

where $\omega = 2\pi f$ is the angular frequency; $\tilde{\boldsymbol{w}}$ is the column vector of the nodal displacement of the plate; $\tilde{\boldsymbol{p}}$ is column the vector of the sound pressure; the matrices $\boldsymbol{K}$, $\boldsymbol{C}$ and $\boldsymbol{M}$ are the stiffness, damping and mass matrices of the structure (subscript s) and the acoustic (subscript a) region, respectively. $\boldsymbol{K}_\mathrm{c}$ and $\boldsymbol{M}_\mathrm{c}$ represent cross-coupling matrices and satisfy the relationship $\boldsymbol{M}_\mathrm{c} = -\rho_0 \boldsymbol{K}_\mathrm{c}^\mathrm{T}$. ρ_0 is the density of air. $\mathrm{j} = \sqrt{-1}$ represents the imaginary unit. $\tilde{\boldsymbol{F}}$ is a column vector of the excitation force. The different forms of the excitation ultimately lead to different responses of the whole system. The problem of noise reduction inside the cavity under force excitation has been investigated previously [23,38]. However, for the noise radiation reduction of the plate-cavity system under interior acoustic excitation, the influence of cavity modes (including non-resonant (0,0,0) cavity modes) on sound radiation cannot be ignored because of the existence of the cavity. In this case, $\tilde{\boldsymbol{F}}_\mathrm{s}$ is the force loading on the structure, and it is equal to 0. The acoustic force $\tilde{\boldsymbol{F}}_\mathrm{a} = \tilde{\boldsymbol{B}} q$ is introduced by the monopole sound source. $\tilde{\boldsymbol{B}}$ is a column vector related to nodal load and q is the amplitude of the monopole sound source.

Based on the modal superposition theory, the structural displacement and the pressure can be expressed as

$$\tilde{\boldsymbol{w}} = \boldsymbol{\Phi}\tilde{\boldsymbol{\lambda}}_\mathrm{s},\ \tilde{\boldsymbol{p}} = \boldsymbol{\Psi}\tilde{\boldsymbol{\lambda}}_\mathrm{a} \tag{2}$$

where $\boldsymbol{\Phi} = [\phi_i]$ $(i = 1, 2, \cdots, m)$ and $\boldsymbol{\Psi} = [\psi_j]$ $(j = 1, 2, \cdots, n)$ are the matrices of modal amplitudes of displacement and pressure, respectively. $\tilde{\boldsymbol{\lambda}}_\mathrm{s} = \left[\tilde{\lambda}_{\mathrm{s}1}\ \tilde{\lambda}_{\mathrm{s}2}\ \cdots\ \tilde{\lambda}_{\mathrm{s}m}\right]^\mathrm{T}$ and $\tilde{\boldsymbol{\lambda}}_\mathrm{a} = \left[\tilde{\lambda}_{\mathrm{a}1}\ \tilde{\lambda}_{\mathrm{a}2}\ \cdots\ \tilde{\lambda}_{\mathrm{a}n}\right]^\mathrm{T}$ are the column vectors of structural and acoustic modal coordinates (or amplitudes), respectively. m and n are the total number of structural modes and cavity modes, respectively.

Then, Eq. (1) can be cast into the following form

$$\left(\begin{bmatrix} \boldsymbol{K}_\mathrm{s} & \boldsymbol{K}_\mathrm{c} \\ 0 & \boldsymbol{K}_\mathrm{a} \end{bmatrix} + \mathrm{j}\omega \begin{bmatrix} \boldsymbol{C}_\mathrm{s} & 0 \\ 0 & \boldsymbol{C}_\mathrm{a} \end{bmatrix} - \omega^2 \begin{bmatrix} \boldsymbol{M}_\mathrm{s} & 0 \\ \boldsymbol{M}_\mathrm{c} & \boldsymbol{M}_\mathrm{a} \end{bmatrix}\right) \cdot \begin{Bmatrix} \boldsymbol{\Phi}\,\tilde{\boldsymbol{\lambda}}_\mathrm{s} \\ \boldsymbol{\Psi}\,\tilde{\boldsymbol{\lambda}}_\mathrm{a} \end{Bmatrix} = \begin{Bmatrix} \boldsymbol{0} \\ \tilde{\boldsymbol{B}}\,q \end{Bmatrix} \tag{3}$$

The unknown quantity in Eq. (3) is the vector of complex modal coordinates $\tilde{\boldsymbol{\lambda}}$. Take the first row of Eq. (3) into account, for the structural domain,

$$\boldsymbol{K}_\mathrm{s}\boldsymbol{\Phi}\,\tilde{\boldsymbol{\lambda}}_\mathrm{s} + \boldsymbol{K}_\mathrm{c}\boldsymbol{\Psi}\,\tilde{\boldsymbol{\lambda}}_\mathrm{a} + \mathrm{j}\omega\boldsymbol{C}_\mathrm{s}\boldsymbol{\Phi}\,\tilde{\boldsymbol{\lambda}}_\mathrm{s} - \omega^2\boldsymbol{M}_\mathrm{s}\boldsymbol{\Phi}\,\tilde{\boldsymbol{\lambda}}_\mathrm{s} = \boldsymbol{0} \tag{4}$$

The structural modal coordinates, $\tilde{\boldsymbol{\lambda}}_\mathrm{s}$, can be expressed as

$$\tilde{\boldsymbol{\lambda}}_\mathrm{s} = -\boldsymbol{T}_\mathrm{s}\boldsymbol{\Phi}^\mathrm{T}\boldsymbol{K}_\mathrm{c}\boldsymbol{\Psi}\,\tilde{\boldsymbol{\lambda}}_\mathrm{a} \tag{5}$$

where $\boldsymbol{T}_\mathrm{s} = \mathrm{diag}[T_{s1},\ T_{s2},\ \cdots,\ T_{sm}]$ is a diagonal transfer matrix, the i^{th} element of which is the transfer function $T_{si} = (\omega_{si}^2 + 2\mathrm{j}\omega\zeta_{si}\omega_{si} - \omega^2)^{-1}$, representing the transfer characteristics of i^{th} structural mode from the modal force induced by the interior acoustic pressure $\tilde{\boldsymbol{p}}$ to the modal coordinate $\tilde{\lambda}_{si}$; ζ_{si} and ω_{si} are the i^{th} modal damping ratio and the modal frequency of the structure, respectively.

For the second row of Eq. (3), in the acoustic domain,

$$\boldsymbol{K}_\mathrm{a}\boldsymbol{\Psi}\,\tilde{\boldsymbol{\lambda}}_\mathrm{a} + \mathrm{j}\omega\boldsymbol{C}_\mathrm{a}\boldsymbol{\Psi}\,\tilde{\boldsymbol{\lambda}}_\mathrm{a} - \omega^2\boldsymbol{M}_\mathrm{a}\boldsymbol{\Psi}\,\tilde{\boldsymbol{\lambda}}_\mathrm{a} - \omega^2\boldsymbol{M}_\mathrm{c}\boldsymbol{\Phi}\,\tilde{\boldsymbol{\lambda}}_\mathrm{s} = \tilde{\boldsymbol{B}}\,q \tag{6}$$

where the coupling term $\omega^2\boldsymbol{M}_\mathrm{c}\boldsymbol{\Phi}\,\tilde{\boldsymbol{\lambda}}_\mathrm{s}$ generated by structural vibrations is negligible because its influence on the pressure response is far small than the acoustic excitation. Similarly, the modal coordinates of the cavity, $\tilde{\boldsymbol{\lambda}}_\mathrm{a}$, are given by

$$\tilde{\boldsymbol{\lambda}}_\mathrm{a} = \boldsymbol{T}_\mathrm{a}\boldsymbol{\Psi}^\mathrm{T}\tilde{\boldsymbol{B}}\,q \tag{7}$$

where $\boldsymbol{T}_\mathrm{a} = \mathrm{diag}[T_{a1},\ T_{a2},\ \cdots,\ T_{an}]$ is a diagonal transfer matrix, the j^{th} element of which is the transfer function $T_{aj} = (\omega_{aj}^2 + 2\mathrm{j}\omega\zeta_{aj}\omega_{aj} - \omega^2)^{-1}$, representing the transfer characteristics of the j^{th} cavity mode from the modal force $\tilde{\boldsymbol{B}}\,q$ to the modal coordinate $\tilde{\lambda}_{aj}$; ζ_{aj} and ω_{aj} are the modal damping ratio and the modal frequency of the cavity, respectively. Considering ζ_{aj} is very small in the air, the influence of the cavity modes on the noise radiation is significant, as it will be seen later.

Substitution of Eq. (7) into Eq. (5) yields

$$\tilde{\boldsymbol{\lambda}}_\mathrm{s} = -\boldsymbol{T}_\mathrm{s}\boldsymbol{\Phi}^\mathrm{T}\boldsymbol{K}_\mathrm{c}\boldsymbol{\Psi}\boldsymbol{T}_\mathrm{a}\boldsymbol{\Psi}^\mathrm{T}\tilde{\boldsymbol{B}}\,q \tag{8}$$

Thus, the complex modal coordinates $\tilde{\boldsymbol{\lambda}}_\mathrm{s}$ can be solved based on FEM.

2.2. Sound radiation theory of the plate-cavity system

According to the Kirchhoff-Helmholtz integral equation [43], the sound pressure at any position in the near or far field can be calculated. The total radiated sound power W [43] is

$$W = \int_{S'} \tilde{I}\,\mathrm{d}S' = \frac{1}{2}\int_{S'} \mathrm{Re}(\tilde{u}^*\,\tilde{p})\mathrm{d}S' = \frac{1}{2}\int_{S} \mathrm{Re}(\tilde{v}_\mathrm{n}^*\,\tilde{p})\mathrm{d}S \tag{9}$$

where $\tilde{I}$ the sound intensity; $\tilde{u}$ is the acoustic particle velocity on the integration interface S' in the near or far field; and $\tilde{v}_\mathrm{n}$ is the structural normal velocity on the radiation interface S. The superscript $*$ denotes complex conjugate and Re the real part.

Given that the radiation surface S can be divided into a grid of N same elements, Eq. (9) is rewritten into the following form [42]

$$W = \frac{1}{2}\int_{S} \mathrm{Re}(\tilde{v}_\mathrm{n}^*\,\tilde{p})\mathrm{d}S = \tilde{\boldsymbol{v}}_\mathrm{n}^\mathrm{H}\boldsymbol{R}\,\tilde{\boldsymbol{v}}_\mathrm{n} \tag{10}$$

where $N \times N$ matrix $\boldsymbol{R}$ is the radiation resistance matrix that is detailed in Appendix A; the column vector $\tilde{\boldsymbol{v}}_\mathrm{n}$ consists of the normal velocities of the N elements for radiation calculation; and the superscript H is the Hermitian transpose operator. Then, Eq. (10) is rewritten as

$$W = \tilde{\boldsymbol{v}}_\mathrm{n}^\mathrm{H}\boldsymbol{P}\boldsymbol{\Lambda}\boldsymbol{P}^\mathrm{T}\tilde{\boldsymbol{v}}_\mathrm{n} = \tilde{\boldsymbol{y}}^\mathrm{H}\boldsymbol{\Lambda}\,\tilde{\boldsymbol{y}} = \sum_{l=1}^{L} x_l\left|\tilde{y}_l\right|^2 \tag{11}$$

where $\tilde{\boldsymbol{y}} = \boldsymbol{P}^\mathrm{T}\tilde{\boldsymbol{v}}_\mathrm{n}$ is the vector of complex amplitude of the "radiation modes" in terms of velocities of the individual radiators [42,44], and $\boldsymbol{P} = [\varphi_l]$ $(l = 1, 2, \cdots, L)$ is a matrix of orthogonal eigenvectors; $\{\varphi_l\}$ is the vector that represents the spatial distribution of the l^{th} radiation mode, which represents specific normal velocity distributions on the panel [45]. L is the total number of the radiation mode. The normal velocity can be calculated from the normal surface displacement $\tilde{\boldsymbol{w}}_\mathrm{n}$, that is, $\tilde{v}_\mathrm{n} = \mathrm{j}\omega\tilde{\boldsymbol{w}}_\mathrm{n} = \mathrm{j}\omega\boldsymbol{\Theta}\,\tilde{\boldsymbol{w}} = \mathrm{j}\omega\boldsymbol{\Theta}\boldsymbol{\Phi}\,\tilde{\boldsymbol{\lambda}}_\mathrm{s}$, where $\boldsymbol{\Theta}$ is a $N \times m$ matrix that transforms the nodal displacement vector $\tilde{\boldsymbol{w}}$ to normal surface displacement vector $\tilde{\boldsymbol{w}}_\mathrm{n}$ and the matrix $\boldsymbol{\Theta}\boldsymbol{\Phi}$ is the modal shape matrix of the radiation surface. The former relationship means that $\tilde{\boldsymbol{w}}_\mathrm{n}$ is obtained by interpolation of nodal displacements of the FEM grid. And $\boldsymbol{\Lambda}$ is a diagonal matrix of eigenvalues x_l. The eigenvalues x_l are proportional to the self-radiation efficiencies σ_l' that represent the radiation capacity of the l^{th} radiation mode as

$$\sigma_l' = 2x_l/\rho_0 c_0 S_0 \tag{12}$$

where c_0 is the velocity of air.

The vector $\tilde{\boldsymbol{y}}$ can be expressed as

$$\tilde{\boldsymbol{y}} = \boldsymbol{P}^\mathrm{T}\tilde{\boldsymbol{v}}_\mathrm{n} = \mathrm{j}\omega\boldsymbol{P}^\mathrm{T}\boldsymbol{\Theta}\boldsymbol{\Phi}\,\tilde{\boldsymbol{\lambda}}_\mathrm{s} \tag{13}$$

Obviously, $\boldsymbol{P}^\mathrm{T}\boldsymbol{\Theta}\boldsymbol{\Phi}$ is a mapping matrix, which maps the structural modal amplitude $\tilde{\boldsymbol{\lambda}}_\mathrm{s}$ to the amplitude of radiation modes $\tilde{\boldsymbol{y}}$ (the $\mathrm{j}\omega$ has been excluded in the mapping matrix).

Substitute Eq. (8) into Eq. (13),

$$\tilde{\boldsymbol{y}} = -\mathrm{j}\omega\boldsymbol{P}^\mathrm{T}\boldsymbol{\Theta}\boldsymbol{\Phi}\boldsymbol{T}_\mathrm{s}\boldsymbol{\Phi}^\mathrm{T}\boldsymbol{K}_\mathrm{c}\boldsymbol{\Psi}\boldsymbol{T}_\mathrm{a}\boldsymbol{\Psi}^\mathrm{T}\tilde{\boldsymbol{B}}\,q \tag{14}$$

The sound power W is rewritten as

$$\begin{aligned} W &= \sum_{l=1}^{L} x_l\left|\mathrm{j}\omega\boldsymbol{P}^\mathrm{T}\boldsymbol{\Theta}\boldsymbol{\Phi}\,\tilde{\boldsymbol{\lambda}}_\mathrm{s}\right|^2 \\ &= \sum_{l=1}^{L} x_l\left|\mathrm{j}\omega\boldsymbol{P}^\mathrm{T}\boldsymbol{\Theta}\boldsymbol{\Phi}\boldsymbol{T}_\mathrm{s}\boldsymbol{\Phi}^\mathrm{T}\boldsymbol{K}_\mathrm{c}\boldsymbol{\Psi}\boldsymbol{T}_\mathrm{a}\boldsymbol{\Psi}^\mathrm{T}\tilde{\boldsymbol{B}}\,q\right|^2 \end{aligned} \tag{15}$$

2.3. Suppression mechanism of noise radiation

Equation (15) indicates that there is a long chain of energy transfer from the sound source inside an acoustic space to the radiated noise, as shown in Fig. 2, different from the case of direct structural force excitation. An acoustic excitation q is placed in an enclosed acoustic space. The acoustic modes $\boldsymbol{\Psi}$ depend only on the geometrical shape of the cavity, but their amplitudes $\tilde{\boldsymbol{\lambda}}_\mathrm{a}$ are determined by the acoustic transfer matrix $\boldsymbol{T}_\mathrm{a}$ and nodal force $\tilde{\boldsymbol{B}}\,q$, as shown in Eq. (7). The structural nodal force is determined by the coupling term $\boldsymbol{\Phi}^\mathrm{T}\boldsymbol{K}_\mathrm{c}\boldsymbol{\Psi}$ and the amplitude of the acoustic modes $\tilde{\boldsymbol{\lambda}}_\mathrm{a}$. Then, the structure subjected to this structural nodal force would vibrate in a superimposed form of some structural modes and the response of each mode is expressed in terms of the modal amplitudes $\tilde{\boldsymbol{\lambda}}_\mathrm{s}$ based on the modal summation [42]. Besides the structural nodal force, the structural transfer matrix $\boldsymbol{T}_\mathrm{s}$ determines

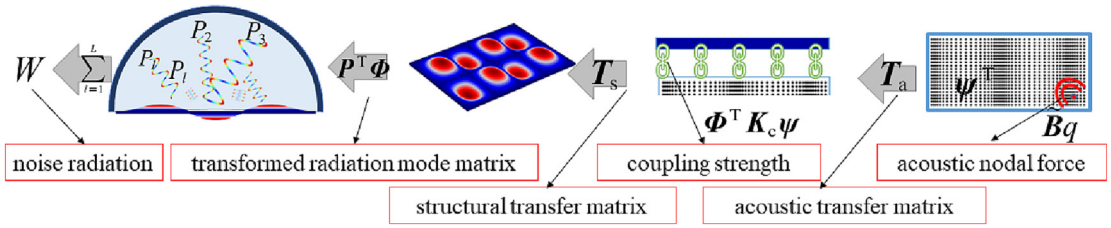

Fig. 2. Schematic of energy transfer.

the values of modal amplitudes $\tilde{\lambda}_s$ as shown in Eq. (5). Above processes are similar to a kind of "frequency filter" of the response, which makes the structural vibration peaks only appear at some certain frequencies, such as the cavity modal frequencies and the structural modal frequencies. Finally, air particles near the vibrated structural surface begin to vibrate, then, noise radiation appears in the near field and far field successively and the peak frequencies of radiation are basically consistent with above filtered frequencies. The sound power of the noise radiation is radiated by a set of radiation modes that are characterized by self-radiation efficiencies σ_l' as shown in Eq. (11) and the complex amplitude of these modes are determined by the modal amplitudes $\tilde{\lambda}_s$ and the mapping matrix $\boldsymbol{P}^{\mathrm{T}}\boldsymbol{\Theta}\boldsymbol{\Phi}$.

Therefore, considering a typical plate-cavity system under interior acoustic excitation, focusing on the noise radiation reduction effect of replacing the flat plate with an ABH plate to form an ABH-cavity system, above parameters can be classified as follows:

a. The invariant parameters. These parameters, such as interior acoustic modal force $\tilde{\boldsymbol{B}}q$ and cavity modal shape $\boldsymbol{\Psi}^{\mathrm{T}}$, are the same for both systems (i.e., plate-cavity and ABH-cavity) in this work. Meanwhile, for plates of the same size, eigenvalues x_l of the diagonal matrix $\boldsymbol{\Lambda}$ and spatial distribution matrix of radiation modes $\boldsymbol{P}$ are also the same. Those parameters are categorized as invariant parameters that will not be considered in this work.
b. The coupling strength $\boldsymbol{\Phi}^{\mathrm{T}}\boldsymbol{K}_{\mathrm{c}}\boldsymbol{\Psi}$, represents the coupling strength between the cavity modal shape $\boldsymbol{\Psi}$ and the structural modal shape $\boldsymbol{\Phi}$. It has been shown in a previous study [38] that coupling coefficients for both systems are very close to each other in the low frequency range.
c. The structural transfer matrix $\boldsymbol{T}_{\mathrm{s}}$ and the acoustic transfer matrix $\boldsymbol{T}_{\mathrm{a}}$. The elements of these matrices represent the transfer characteristics of their own modes from the modal force to their own modal coordinates. And the values of elements of transfer matrices $\boldsymbol{T}_{\mathrm{s}}$ and $\boldsymbol{T}_{\mathrm{a}}$ are decided by their corresponding modal damping ratio ζ_{s} and ζ_{a}. Compared with the cavity modal damping ratio ζ_{a}, the structural one ζ_{s} is much easier to manipulate. Massive damping layer are usually used to obtain a high value of ζ_{s} in traditional passive control, but for ABHs, only a small amount damping layer need to be added in the center of the ABH region to achieve the high damping loss.
d. The mapping matrix $\boldsymbol{P}^{\mathrm{T}}\boldsymbol{\Theta}\boldsymbol{\Phi}$. The element $\{\varphi_l\}^{\mathrm{T}}\boldsymbol{\Theta}\{\phi_i\}$ of the matrix $\boldsymbol{P}^{\mathrm{T}}\boldsymbol{\Theta}\boldsymbol{\Phi}$ denotes the contribution of the i^{th} structural mode to the l^{th} radiation mode. In order to obtain a reduced noise radiation, considering that the matrix $\boldsymbol{P}$ of radiation modal distributions is unalterable because the size of the plate is determinate, it is viable to lower the absolute value of the element $\{\varphi_l\}^{\mathrm{T}}\boldsymbol{\Theta}\{\phi_i\}$ by changing forms of the structural modal shape of the radiation surface $\boldsymbol{\Theta}\boldsymbol{\Phi}$. It should be noted that sound power W is a sum of the product of the mapping matrix $\boldsymbol{P}^{\mathrm{T}}\boldsymbol{\Theta}\boldsymbol{\Phi}$ and the complex structural modal coordinate $\tilde{\lambda}_s$. A cross-cancellation effect or a cross-enhancement caused by the mismatch/match between the mapping coefficients and the structural modal coordinates will weaken or enhance the sound power accordingly.

As indicated above, the noise radiation of the ABH-cavity system is suppressed in two ways in this work.

One is to lower the structural transfer function by increasing the structural damping loss ζ_{s}. For the ABH structure, a lager ζ_{s} is achievable by adding a small amount of damping layer in the center of ABH structures due to the damping enhancement of ABH plates that has been validated as mentioned above.

The other is to reduce the absolute value of the mapping coefficient $\{\varphi_l\}^{\mathrm{T}}\boldsymbol{\Theta}\{\phi_i\}$ by changing forms of the structural modal shape $\boldsymbol{\Phi}$. It should be pointed out that generating a series of local resonance modes in the central area of ABHs is one of the remarkable characteristics of ABH structures. Therefore, rearranging the number and distribution of ABHs can change the form of the modal shapes $\boldsymbol{\Phi}$. For a simply supported rectangular uniform plate, the analytical solution of radiation efficiencies of structural modes indicates that structural mode (2,2) and (2,1) enable a relatively low radiation efficiency than mode (1,1) at low frequencies [46]. Combining these two concepts, two ABH plates whose shapes are very similar to the mode (2,1) and (2,2) are designed to reduce the sound power in the following sections.

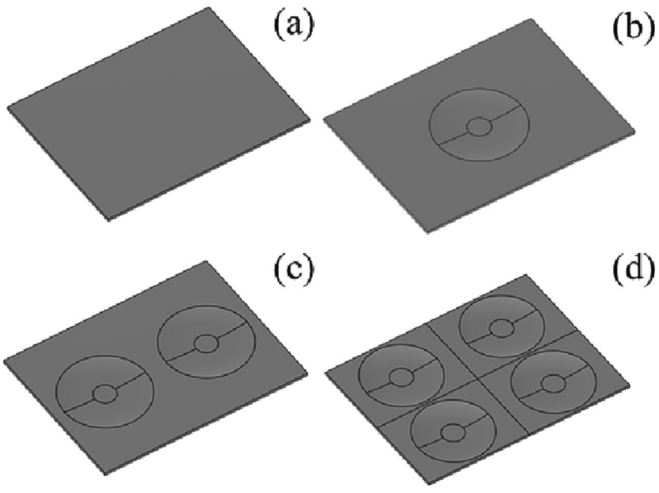

Fig. 3. Four plates under investigation. (a) UNI; (b) 1-ABH; (c) 2-ABH; (d) 4-ABH.

Table 1
List of cases.

Cases	Plate	Loss factor of DL	Purpose
1	UNI	0.1	Reference results
2	1-ABH	0.1	
3	UNI	0.3	Lowering the magnitude of structural transfer function
4	1-ABH	0.3	
5	2-ABH	0.3	Manipulating the mapping matrix
6	4-ABH	0.3	

3. FE model and results

3.1. FE model

To verify above mentioned suppression mechanism of noise radiation in an ABH-cavity system, one uniform plate and three different ABH plates with the same plate thickness h_1 are built, named UNI, 1-ABH, 2-ABH and 4-ABH, respectively, as shown in Fig. 3. Six cases of above plates are created and listed in Table 1, details of each case are given below.

In case 1, a UNI plate is coated with a damping layer whose loss factor of damping layer (DL) is 0.1. And the UNI plate is replaced by the 1-ABH plate in case 2. The detailed analyses of case 1 and 2 are shown in section 3.2 as a reference for latter cases. In case 3, the loss factor of damping layer of the UNI plate system is increased to 0.3 and other parameters remain unchanged so it is comparable with case 1. Similarly, in case 4, the loss factor of damping layer of the 1-ABH plate system is tripled to be compared with case 2. Case 3 and 4 are carried out for demonstrating the suppression mechanism of noise radiation by decreasing the magnitude of structural transfer functions. In case 5 and 6, the loss factor of the damping layer is kept at 0.3 but the ABH plate is designed differently. The numbers of ABHs in the plate are increased to 2 and 4 to form the 2-ABH and 4-ABH model, whose modal shapes correspond to structural mode (2,1) and mode (2,2) respectively. This design is inspired from the above analysis that those two structural modes show lower radiation efficiency than mode (1,1). Therefore, the suppression mechanism of noise radiation is investigated by manipulating the mapping matrix $\boldsymbol{P}^{\mathrm{T}}\boldsymbol{\Theta}\boldsymbol{\Phi}$ in case 5 and 6.

3.1.1. Geometrical and material parameters of ABHs

The geometrical parameters of ABHs are shown in Fig. 4. For an ABH-cavity system, the thickness of the uniform part of the ABH is denoted as h_1, the thickness power-law profile of the ABH part is described as

$$h(r) = \begin{cases} h_0, & 0 \leqslant r \leqslant r_0 \\ a(r - r_0)^2 + h_0, & r_0 \leqslant r \leqslant r_1 \end{cases} \tag{16}$$

where h_0 represent the residual thickness; a is a constant; r_0 and r_1 symbolize the radius of the central platform and the whole ABH area, respectively. A damping layer with a radius of r_d and a thickness of h_d, is concentrically attached on the backside of the ABH region, as shown in Fig. 4.

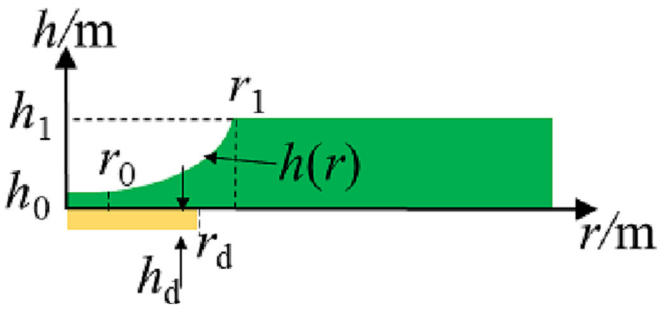

Fig. 4. Geometrical parameters of ABHs.

The geometrical and material parameters of the FE model are illustrated in Table 2. The 1-ABH and 2-ABH has the same ABH curves described above, while the profile curve of the 4-ABH has shrunk slightly to a = 1.92 and r_1 = 0.07 m because of the limitation of the structural size. Other parameters remain the same as shown in Table 2. E is the Young's modulus; μ is the Poisson's ratio; η is the loss factor; ρ is the density. And subscripts AL and d denote the aluminum plate and the damping layer, respectively. The same damping layers are added in the center of ABH regions for all ABH plates in this work.

3.1.2. Boundary conditions and meshes of FE model

A FE model of a cavity-plate-far-field system is established as shown in Fig. 5(a). Given the existence of the damping layer, the complex modal analysis of the structural domain is firstly done in ABAQUS, then the result is imported into LMS.virtual Lab (Siemens PLM Software, LMS, Belgium) to complete the calculation of structural vibrations and acoustic response. As shown in Fig. 5 (a), a rectangular cavity with a dimension of 0.40 m × 0.30 m × 0.18 m is built with one of the bottom corners as the origin of the coordinate system. The acoustic excitation is introduced by a monopole sound source with a fixed amplitude of $q = 1$ kg/s^2. It is applied at (0.02 m, 0.02 m, 0.02 m), which, as shown in Fig. 5(a), is close to the corner of the rectangular acoustic space. This is considered to be an ideal location to drive the rectangular space when it is desirable to introduce sound [46], because every cavity mode has a pressure antinode at corners.

The boundary conditions of the whole system are shown in Fig. 5(b). First and foremost, to ensure the normal fluid velocity equals the normal structural velocity along the vibro-acoustic coupling interface, vibro-acoustic coupling boundary conditions are applied on both the cavity-ABH interface and ABH-far-field interface. For boundary conditions of the structural domain, edges of the plate are clamped. For boundary conditions of the acoustic domain, to realize a perfect sound absorption in the far-field, the automatically matched layer boundary condition (AML BC) in LMS.virtual Lab is set on the convex interface of far-field mesh. The AML interface satisfies the Kirchhoff radiation condition. And the remaining five cavity walls are assumed as perfectly rigid walls to prevent flanking sound leakage.

All meshes of the FE model are generated in ABAQUS. For the acoustic meshes shown in Fig. 5(a), more than six elements (AC3D8, an 8-node linear acoustic brick) per local acoustic wavelength are used to guarantee the computation accuracy in acoustic analysis. The corresponding element size of the cavity mesh is 5.7 mm. Finer meshes are generated for the far-field part. For the structural meshes shown in Fig. 5(c)∼(e), C3D20 solid elements (a second-order element with 20 nodes) are used to discretize the ABH plate. Since the critical frequency [37] (calculated by $f_{\mathrm{crit}} = c_0^2/(2\pi h_0)\sqrt{12\rho_{\mathrm{AL}}(1-\mu_{\mathrm{AL}}^2)/E_{\mathrm{AL}}}$) of the uniform plate is about 2405 Hz, the interested frequency range in this study is set from 10 to 2500 Hz. So, the size of elements at the central area of the ABH plate are carefully set so that there are more than ten elements per local wavelength to satisfy the calculation accuracy requirement. The resulting total element number of the 1-ABH, 2-ABH and 4-ABH plate is 9728, 12644 and 21712, respectively. For comparison purpose, the UNI plate is modelled with a total element number of 4178.

3.2. Preliminary results and discussions

In order to better discuss the acoustic and vibration characteristics of the plate-cavity system, several evaluation parameters are introduced as follows.

Table 2
Geometrical and material parameters.

Geometry		Material		
a = 4/3	r_0 = 0.02 m	E_{AL} = 70 GPa	E_d = 0.1 GPa	ρ_0 = 1.29 kg/m^3
h_0 = 0.0002 m	r_1 = 0.08 m	μ_{AL} = 0.33	μ_d = 0.45	c_0 = 343 m/s
h_1 = 0.005 m	r_d = 0.03 m	ρ_{AL} = 2700 kg/m^3	ρ_d = 1780 kg/m^3	
	h_d = 0.002 m	η_{AL} = 0.001	η_d = 0.1	

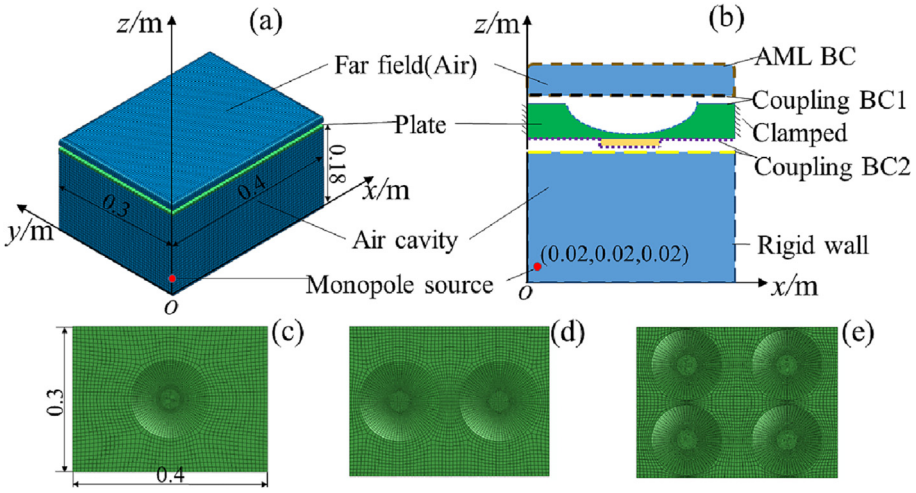

Fig. 5. Configuration of the cavity-plate-far field system. (a) FEM model; (b) boundary conditions; (c) 1-ABH mesh; (d) 2-ABH mesh; (e) 4-ABH mesh.

The structural velocity at any position can be easily accessed from the FEM results. The mean quadratic velocity (represents the level of vibrations, Lv) of the plate at the radiation interface S is calculated by [38]

$$\mathrm{Lv} = 10\lg\frac{\langle v^2\rangle}{\langle v_{\mathrm{ref}}^2\rangle} \tag{17}$$

where $\langle v^2\rangle = \frac{1}{2S}\int_S \tilde{v}_n\tilde{v}_n^* dS$; the reference normal velocity $v_{\mathrm{ref}} = 1$ m/s. S is the area of the vibration interface.

The sound power level (SWL) can be defined as

$$\mathrm{SWL} = 10\lg\frac{W}{W_{\mathrm{ref}}} \tag{18}$$

where the sound radiation W can be derived through the AML interface; and the reference sound power in air $W_{\mathrm{ref}} = 1\times10^{-12}$ W.

The radiation efficiency σ of panels, which represents the radiation capacity of the whole vibrating interface, can be defined as follows [31]

$$\sigma = \frac{W}{\rho_0 c_0 S\langle v^2\rangle} \tag{19}$$

Firstly, for UNI and 1-ABH plates in case 1 and 2, results of the noise radiation and structural vibrations are discussed. The SWLs radiated by both 1-ABH and UNI plates are compared in Fig. 6 in narrow band and 1/3 octave frequency band. Generally, the noise radiation of the 1-ABH system is noticeably lower than the UNI one above 1000 Hz center frequency, but the 1-ABH plate does not always exhibit a reduced SWL below 1000 Hz as illustrated in Fig. 6(b). Specific analyses of different frequency ranges are as follows.

It is found that the 1st modal frequencies of the 1-ABH plate, the UNI plate and the cavity are 366 Hz, 387 Hz and 428 Hz, respectively. Hence, below 366 Hz, the structural vibrations and the sound radiation are affected by the (0,0,0) cavity mode. In the low frequency range, the masses of the plates play a significant

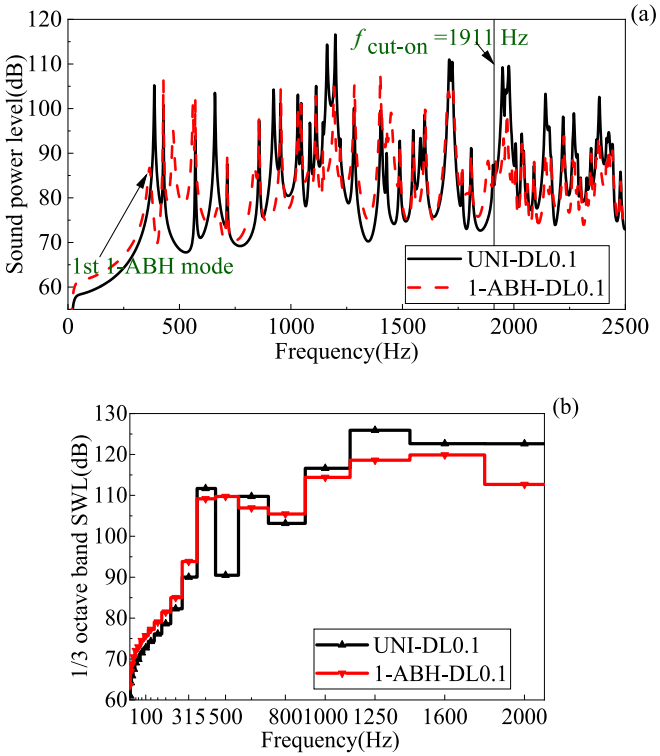

Fig. 6. SWL of plates. (a) narrow band; (b) 1/3 octave frequency band. DL0.1 denotes that the loss factor of damping layers is 0.1.

role on structural vibrations. Comparing with the UNI plate, the mass of the ABH system is smaller, that causes a much higher SWL below 366 Hz. The similar phenomena has been reported in a literature [41] and it is the limitation of ABHs at lower frequen-

cies where the local modes of ABHs do not exist. And an alternative way to suppress structural vibrations at these lower frequencies is to attach periodic local resonators to form a metamaterial ABH (MMABH) plate [47].

On the other hand, systematic ABH effect can be expected above the cut-on frequency, above which the local resonance modes concentrate the vibration energy in the central area of ABHs [23]. According to [48], the cut-on frequency of the 1-ABH plate is 1911 Hz in this work, that is calculated by

$$f_{\text{cut-on}} = \frac{2\pi h_1}{(2r_1)^2}\sqrt{\frac{E_{\text{AL}}}{12\rho_{\text{AL}}(1-\mu_{\text{AL}}^2)}} \tag{20}$$

Above this frequency, the structural bending wavelengths are smaller than the ABH outer diameter $(2r_1)$. Consequently, the SWL of the 1-ABH plate is much lower than the UNI plate in both narrow band and 1/3 octave frequency band beyond the cut-on frequency as shown in Fig. 6.

The ABH effect begins to take effect from the 1st modal frequency of 1-ABH plate (366 Hz), but it will not produce systemic effects until the cut-on frequency 1911 Hz. Specially, as shown in Fig. 6(b), from 366 Hz to 1000 Hz, the 1-ABH plate exhibits a higher SWL at some frequency ranges. In this frequency range, the vibration comparison between the ABH plate and UNI one is shown in Fig. 7. The green color bars correspond to cavity modal frequencies. As expected, peak frequencies of structural vibrations are affected by above two kinds of dominant modes: the structural modes and the cavity modes. For the structural modes, the material parameters, such as the density, elastic modulus and stiffness, play a significant role in determining the structural modes of a structure. Regarding the acoustic modes, they are primarily determined by the geometry and size of the cavity with boundaries assumed to be acoustically rigid. The vibration level of the ABH plate at cavity modal frequencies is obviously higher than the reference one. Given that the SWL result of 1/3 octave frequency band is an accumulative outcome of the whole bandwidth, the higher vibrations at any frequencies are disadvantageous for the reduction of noise radiation in far-field.

The further analysis on the reduction of the vibrations and radiation for the ABH plate in this frequency range is carried out in following sections.

4. Suppression mechanism of noise radiation in an ABH-cavity system

As mentioned in section 2.3, the noise radiation of the plate-cavity system is suppressed in two ways: One is to lower the magnitude of structural transfer function; the other is to change the mapping matrix $\boldsymbol{P}^{\mathrm{T}}\boldsymbol{\Theta}\boldsymbol{\Phi}$. The corresponding numerical results are shown in section 4.1 and 4.2.

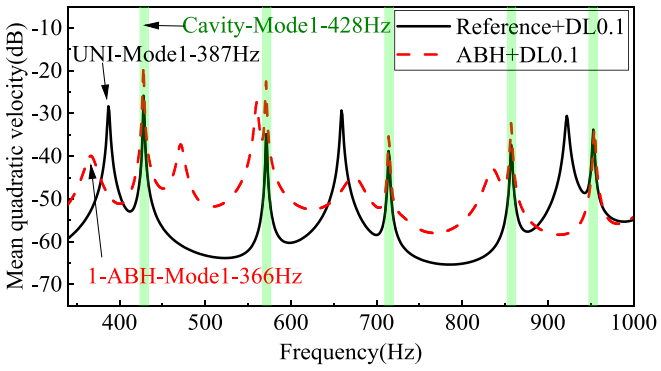

Fig. 7. Vibration comparison between the 1-ABH plate and the UNI plate.

4.1. Decreasing the magnitude of the structural transfer function

UNI and 1-ABH plates coated with two different loss factors η_{d} (case 1 ~ 4) are compared to verify the suppressed mechanism by decreasing the magnitude of the structural transfer function. The corresponding SWL results are compared in Fig. 8. The SWL of the UNI plate has little change when η_{d} is triply increased. As expected, the 1-ABH plate achieves a significant SWL reduction.

As mentioned that other parameters are unchanged or of little influence, the sound radiation is mainly decided by the structural transfer matrix $\boldsymbol{T}_{\text{s}}$. The i^{th} structural transfer function T_{si} is inverse to the modal loss ratio ζ_{si}. Due to the damping enhancement effect of ABH structures as shown in Fig. 9, the modal damping ratio of the ABH plate is much higher than the UNI one, which means the ABH plate accesses a smaller T_{si}. Then, the corresponding vibration suppression of 1-ABH plate is achieved as shown in Fig. 10. Thus, the noise radiation of 1-ABH plate system can be suppressed by decreasing the values of elements of transfer matrix $\boldsymbol{T}_{\text{s}}$. For example, due to this mechanism, at the 1st structural modal frequency (366 Hz for the 1-ABH plate and 388 Hz for the UNI plate), the modal loss factor of 1-ABH-Mode1 increases from 0.036 to 0.105 where the loss factor of the damping layer is significantly increased. And the corresponding structural vibration level and sound power level obtain a reduction of 8.5 dB simultaneously. But for the UNI plate, its structural modal loss factor shows little change with the additional damping material, consequently, the vibration level and sound power level show no noticeable change.

4.2. Influence of the mapping matrix

Based on the theoretical analysis mentioned in section 2.3, lowering the values of elements of the mapping matrix $\boldsymbol{P}^{\mathrm{T}}\boldsymbol{\Theta}\boldsymbol{\Phi}$ is an

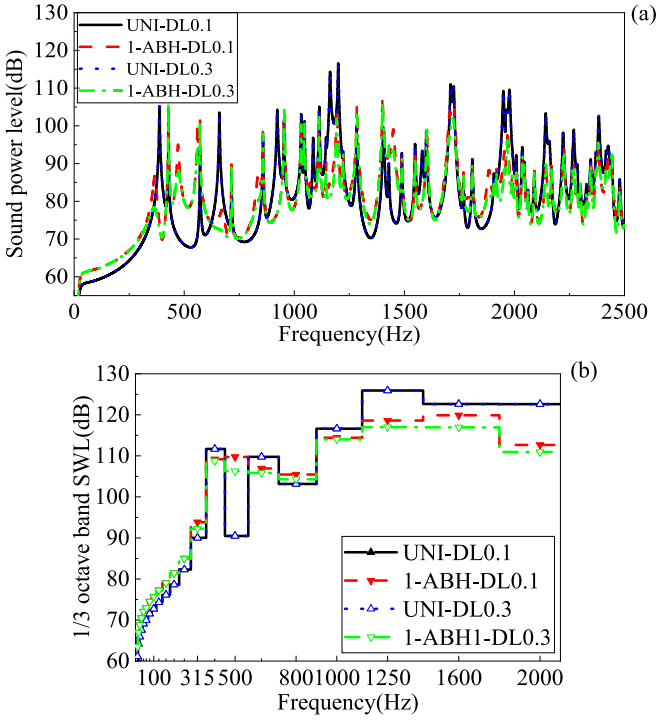

Fig. 8. SWL of plates with different loss factors of the damping layer. (a) narrow band; (b) 1/3 octave frequency band.

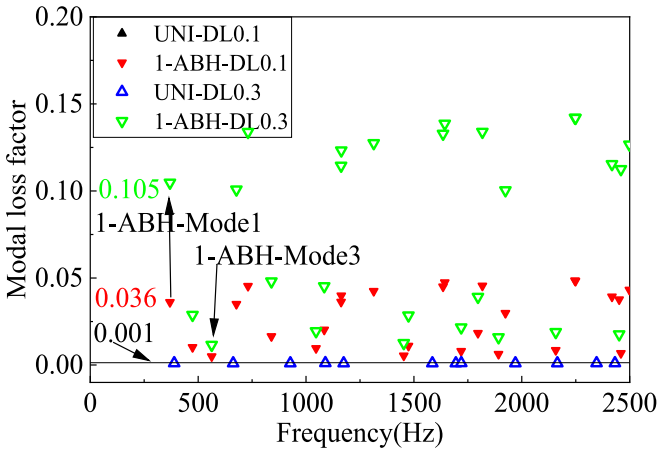

Fig. 9. Modal loss factor as the loss factor of the damping layer varies.

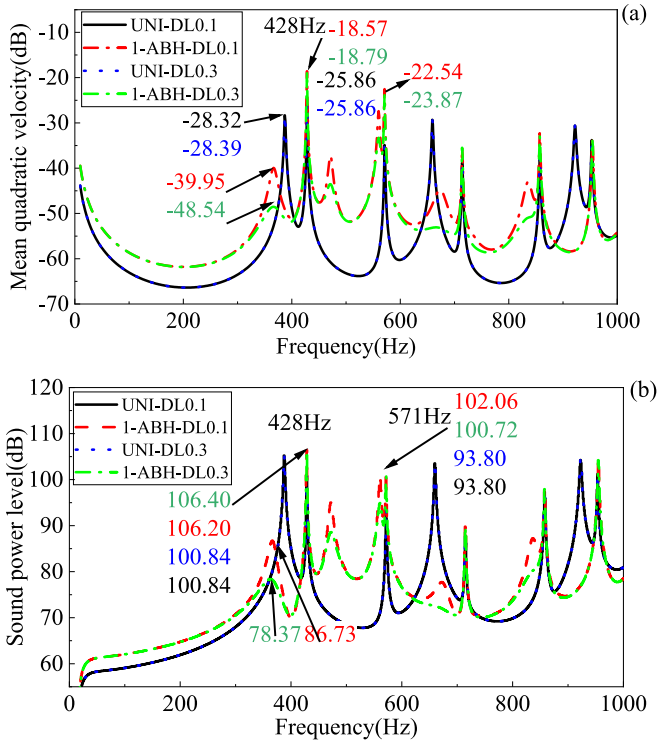

Fig. 10. Vibrations and sound radiation of plates under 1000 Hz. (a) Lv; (b) SWL.

optional way to suppress the noise radiation. The 2-ABH and 4-ABH plates (case 5 and 6) are investigated for demonstrating this mechanism. For comparison, results of UNI and 1-ABH plates (case 3 and 4) are provided.

The results of the SWL, the structural vibration level and the radiation efficiency of above plates are illustrated in Fig. 11. At most modal frequencies, in terms of the vibration levels, the values of mean quadratic velocity of 2-ABH and 4-ABH plates are larger than the UNI plate. But 2-ABH and 4-ABH plates radiate less radiated sound energy into far-field. In other words, the radiation efficiencies σ of the 2-ABH and 4-ABH plates are decreased as shown in Fig. 11(d). For example, at 428 Hz (the 1st modal frequency of the cavity), 2-ABH plate shows the highest vibration and the lowest SWL as compared with other plates. However, the situation reverses at some modal frequencies, such as the 1st structural modal frequency. This reduction or enhancement mechanism of

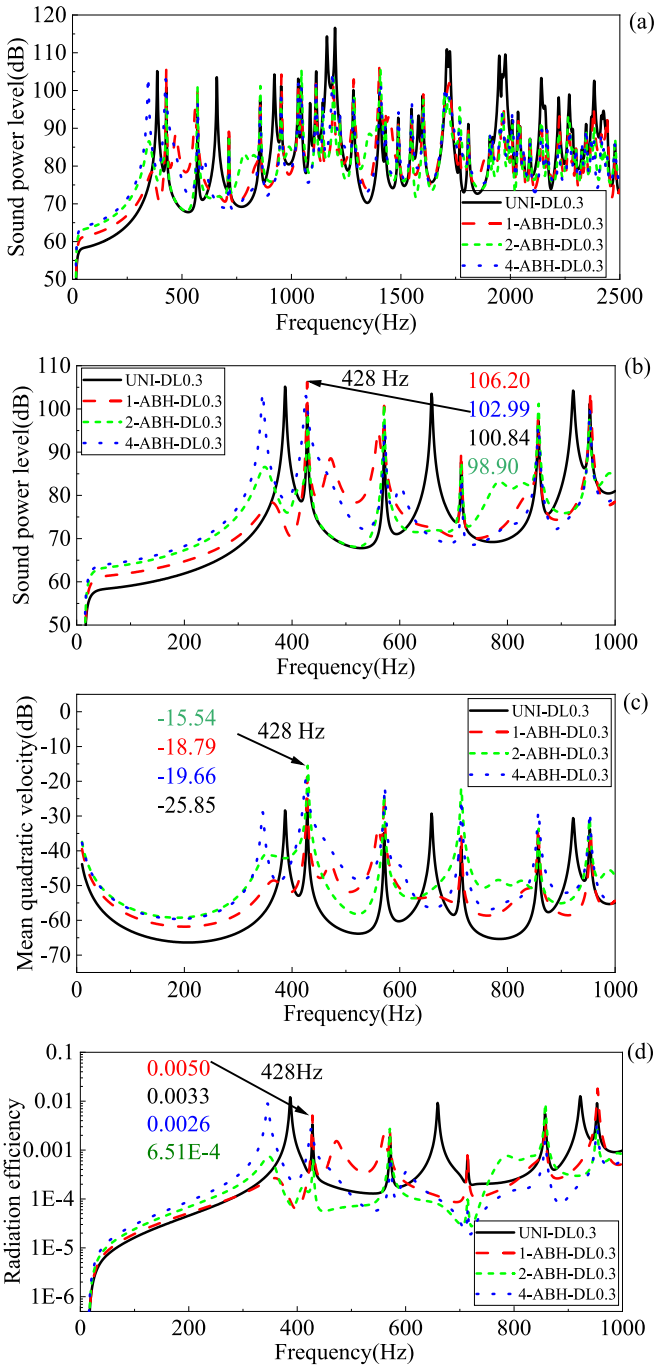

Fig. 11. Vibrations and sound power levels of different ABH designs. (a) SWL in 10–2500 Hz; (b) SWL in 10–1000 Hz; (c) Lv; (d) radiation efficiency.

SWL and radiation efficiency of ABH plates is discussed in detail as follows.

Given the orders of the structural modes are massive because of the degrees of freedom of systems, mode truncation technique is used for analyzing the mapping matrix $\boldsymbol{P}^{\mathrm{T}}\boldsymbol{\Theta}\boldsymbol{\Phi}$ at a specific frequency. For example, at 428 Hz (the 1st cavity modal frequency), considering the first 4, 8, 11 and 16 structural modes of UNI, 1-ABH, 2-ABH and 4-ABH plates is accurate enough for analysis. For radiation modal shapes, only the lower radiation modes have much influence on sound radiation at low frequencies. Therefore, only the first 5 radiation modes are taken into account at 428 Hz. The detail of truncation of modes is shown in the Appendix B.

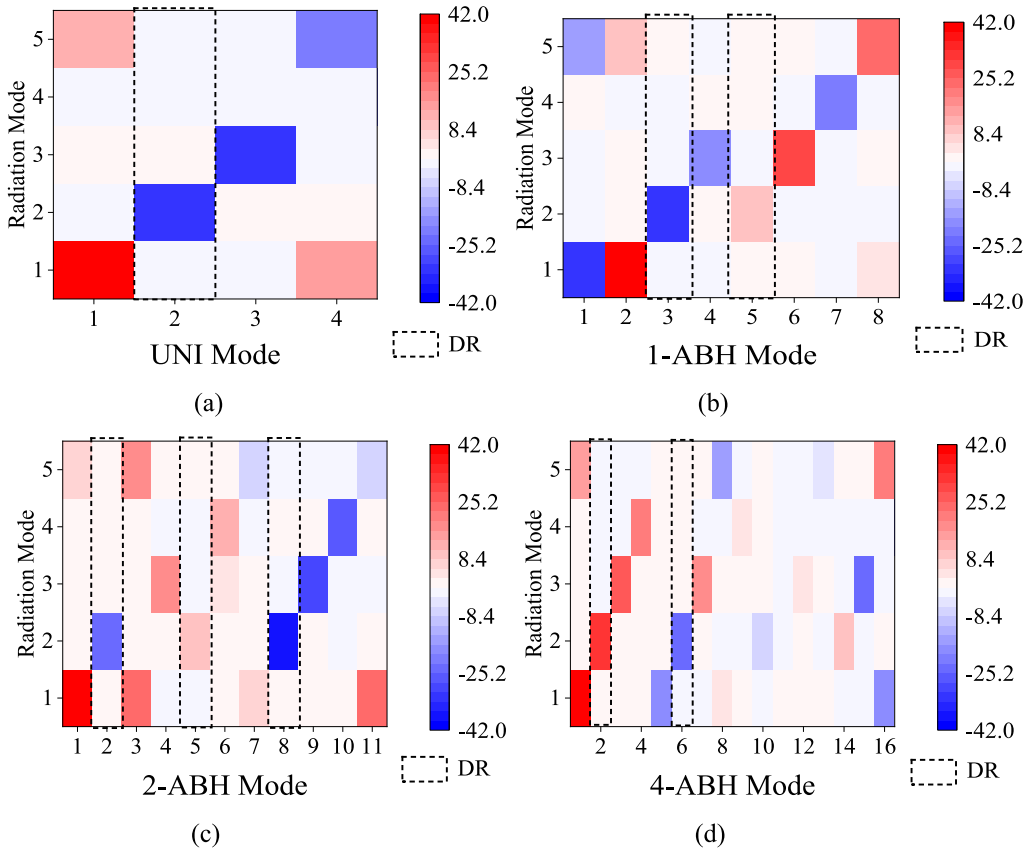

Fig. 12. Mapping matrix of plates. (a) UNI; (b) 1-ABH; (c) 2-ABH; (d) 4-ABH. DR denotes the dominant region.

Table 3
Modal coordinates and mapping coefficients of plates at 428 Hz.

Structural modes		Modal coordinates (10^{-5})		Mapping coefficients $\{\varphi_2\}^{\mathrm{T}}\mathbf{\Theta}\{\phi_i\}$
		Complex form	Absolute value	
Case 3	UNI-Mode2	1.60–3.00j	3.40	−32.50
Case 4	1-ABH-Mode3	−2.80–5.50j	6.17	−31.53
	1-ABH-Mode5	0.40 + 0.60j	0.72	10.31
Case 5	2-ABH-Mode2	−4.10 + 4.50j	6.09	−23.01
	2-ABH-Mode8	0.40–1.10j	1.17	−36.48
	2-ABH-Mode5	−0.10 + 0.50j	0.51	10.31
Case 6	4-ABH-Mode2	3.00 + 2.50j	3.91	33.59
	4-ABH-Mode6	−0.10 −0.60j	0.61	−23.76

Based on above truncation principle, the related mapping matrix $\boldsymbol{P}^{\mathrm{T}}\mathbf{\Theta}\mathbf{\Phi}$ of plates at 428 Hz are illustrated in Fig. 12. The black dashed lines in Fig. 12 represent a dominant region (DR) in which both of modal coordinates $\tilde{\lambda}_{si}$ and self-radiation efficiencies get quite higher values simultaneously. The related results are summarized in Table 3. As illustrated in Table 3, the mapping coefficients of the dominating structural modes of 2-ABH (2-ABH-Mode2 and 2-ABH-Mode5) are very small, which is one of the reasons that the SWL and radiation efficiency σ of the 2-ABH plate simultaneously get a reduction at 428 Hz.

On the contrary, a higher mapping coefficient would enhance the noise radiation. The absolute value of the coefficient $\{\varphi_2\}^{\mathrm{T}}\mathbf{\Theta}\{\phi_i\}$ of 4-ABH-Mode2 is 33.59 and it is larger than the coefficient $\{\varphi_2\}^{\mathrm{T}}\mathbf{\Theta}\{\phi_i\}$ of UNI-Mode2. Thus, 4-ABH plate exhibits a SWL enhancement of 2.1 dB as compared with UNI plate shown in Fig. 11.

Meanwhile, the cross-cancellation or cross-enhancement effect caused by the mismatch/match between the mapping coefficients and the structural modal coordinates will weaken or enhance the sound power accordingly. For instance, for the 2-ABH plate, the real and imaginary parts of the modal coordinates between 2-ABH-Mode2 and 2-ABH-Mode8 are in contrary signs (the vibrations are in nearly opposite phase), whilst the coefficients ($\{\varphi_2\}^{\mathrm{T}}\mathbf{\Theta}\{\phi_2\} = -23.01$ and $\{\varphi_2\}^{\mathrm{T}}\mathbf{\Theta}\{\phi_8\} = -36.48$) are in the same sign, which means that a numerical cancelation is obtained when a summation is executed as suggested by Eq. (15). But for 1-ABH plate, the situation is in reverse, which leads to a cross-enhancement effect.

At other frequencies, above analysis remains applicable. For results of the cavity-mode3-714 Hz, the vibration level of the 4-ABH plate is about 13 dB higher than the UNI plate, but the SWL of the 4-ABH plate system is 3.54 dB lower as shown in Fig. 11 (b) and (c). Thus, the corresponding radiation efficiency of the 4-ABH plate is smaller (6.45×10^{-5} for the 4-ABH plate and 7.03×10^{-4} for the UNI plate) as shown in Fig. 11(d). As compared with the UNI plate, the smaller SWL and radiation efficiency of the 4-ABH plate are realized at 714 Hz and the detailed results are shown in Table C1 in Appendix C. Above analysis focuses on the noise radiation suppression of the 1st and the 3rd cavity modes, however, it should be noted that the noise radiation at any frequency (other cavity modal frequencies under the cut-on frequency especially, as shown in Fig. D1 in Appendix D) will be suppressed by manipulating the mismatch if a further optimization analysis of rearranging the number and distribution of ABHs is carried out.

5. Conclusions

This paper focuses on investigating the suppression mechanism of noise radiation in the ABH-cavity system when a sound source is positioned within a rectangular air cavity. The objective is to examine the underlying mechanism of the coupling between the acoustic space and the ABH plate. The investigation is carried out through theoretical analysis, and the findings are validated numerically using the finite element method within the lower frequency range.

For the coupled plate-cavity system under the interior acoustic excitation, the noise radiation in air is related to both the structural modes and the cavity modes. Theoretical analysis shows that the structural transfer matrix and the mapping matrix are two key factors to reduce the noise radiation of the ABH-cavity system. To verify the theory, finite element models of the ABH-cavity system as well as uniform-plate-cavity system are built. Due to the damping enhancement of ABHs, a smaller structural transfer function can be obtained by increasing the loss factor of the damping layer. The results show the structural vibrations and sound power of ABH plates are reduced as expected. As for the mapping matrix that is the product of radiation modal shapes and structural modal shapes of the radiation surface, its influence on suppression of noise radiation can be explained by two factors. The first one is the small absolute value of the mapping coefficient $\{\varphi_2\}^{\mathrm{T}}\boldsymbol{\Theta}\{\phi_i\}$. The other is the cross-cancellation effect caused by the mismatch between the mapping coefficients and the structural modal coordinates. ABH-cavity systems with varying number of ABHs are constructed to demonstrate a simple solution of manipulating the mapping matrix to achieve enhanced noise radiation suppressing effect by changing forms of the structural modal shape $\boldsymbol{\Phi}$. Numerical analyses show that reduced radiation efficiency and less radiated noise of 2-ABH and 4-ABH plates can be achieved at some frequencies because of the changed mapping matrix.

In general, this work indicates that further optimization analysis of rearranging the number and location of ABHs is a feasible direction for noise radiation suppression of the plate-cavity system.

CRediT authorship contribution statement

Hanfeng Ye: Conceptualization, Formal analysis, Investigation, Writing – original draft. **Hongli Ji:** Conceptualization, Funding acquisition, Writing – review & editing. **Chaoyan Wang:** Validation, Resources, Data curation. **Chongcong Tao:** Investigation, Visualization. **Li Cheng:** Methodology, Funding acquisition. **Jinhao Qiu:** Methodology, Funding acquisition, Supervision, Project administration.

Data availability

Data will be made available on request.

Declaration of Competing Interest

The authors declare that they have no known competing financial interests or personal relationships that could have appeared to influence the work reported in this paper.

Acknowledgments

This work is partially supported by the National Natural Science Foundation of China (Nos. 52022039, U2241261, 52241103), and a Project Funded by the Priority Academic Program Development of Jiangsu Higher Education Institutions.

Appendix A: Radiation resistance matrix

For the convenience of calculation, the coupling interface S can be divided into a grid of N same elements as shown in Fig. A1. The $\tilde{v}_i$ and $\tilde{p}_i$ are structural normal velocities and the pressures of the corresponding elements at their center position. The area of each element is A_e.

Thus, impedance matrix $\tilde{\boldsymbol{Z}}$ is a $N \times N$ matrix. Because of reciprocity, $\tilde{\boldsymbol{Z}}$ is symmetric and $\tilde{Z}_{ij}(\omega) = (j\omega\rho_0 A_e/2\pi d_{ij})e^{-jk'd_{ij}}$. And the relationship between radiation resistance matrix $\boldsymbol{R}$ and $\tilde{\boldsymbol{Z}}$ is given by

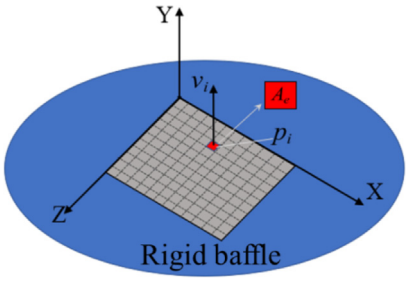

Fig. A1. The subdivision of the coupling interface.

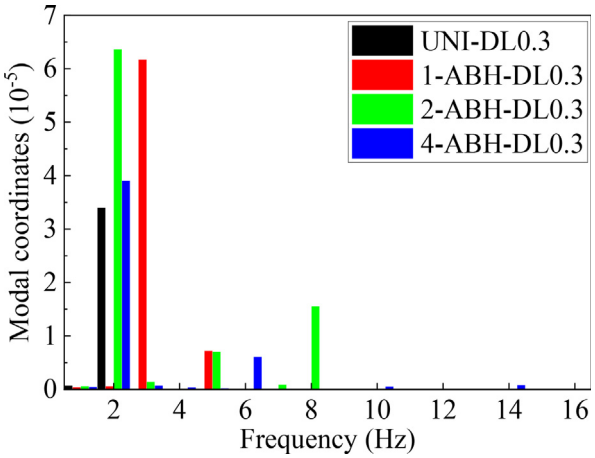

Fig. B1. Modal coordinates of plates at 428 Hz.

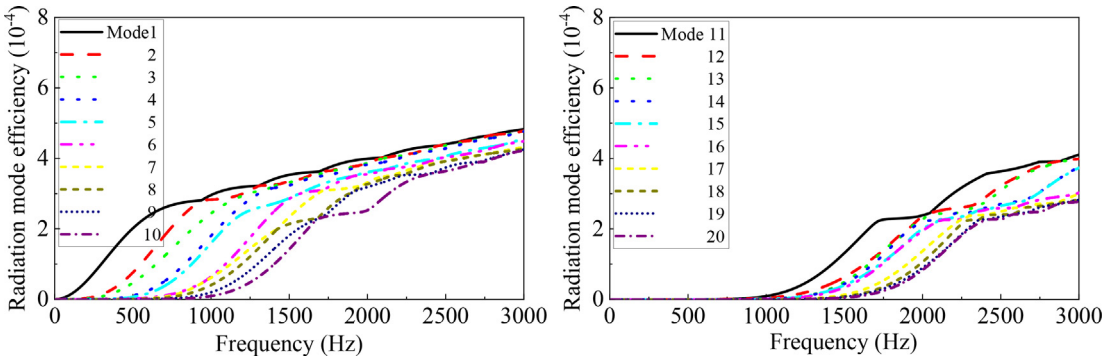

Fig. B2. Self-radiation efficiency σ' of first 20 radiation modes.

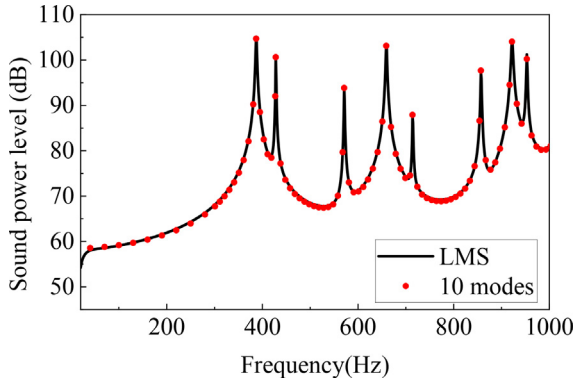

Fig. B3. Comparison of SWL between the first 10 modes and the LMS results.

$$\boldsymbol{R} = \frac{1}{2} A_e Re(\tilde{\boldsymbol{Z}}) \tag{A1}$$

where $\boldsymbol{R}$ can be expressed by [44]

$$\boldsymbol{R} = \frac{\omega^2 \rho_0 A_e^2}{4\pi c_0} \begin{bmatrix} 1 & \frac{\sin(k' d_{12})}{k' d_{12}} & \cdots & \frac{\sin(k' d_{1N})}{k' d_{1N}} \\ \frac{\sin(k' d_{21})}{k' d_{21}} & 1 & \cdots & \vdots \\ \vdots & \vdots & \ddots & \vdots \\ \frac{\sin(k' d_{N1})}{k' d_{N1}} & \cdots & \cdots & 1 \end{bmatrix} \tag{A2}$$

where d_{ij} is the distance between the centers of the i^{th} and j^{th} elements. k' is the wavenumber. And $\boldsymbol{R}$ has an eigenvalue/eigenvector decomposition such as

$$\boldsymbol{R} = \boldsymbol{P} \boldsymbol{\Lambda} \boldsymbol{P}^{\mathrm{T}} \tag{A3}$$

Appendix B: Truncation of structural modes and the radiation modes

For the uniform plate, only the 4 lowest orders of structural modes are considered because the 4th structural modal frequency is 1090 Hz and higher order modes have little influence on the structural vibrations at 428 Hz. For the same reason, the first 8, 11 and 16 structural modes are taken into account for 1-ABH, 2-ABH and 4-ABH plates, respectively. And only some modes have a contribute to the structural vibrations at 428 Hz, as shown in Fig. B1.

The self-radiation efficiencies $\sigma_l' = 2x_l/\rho_0 c_0 S_0$ remain unchanged for plates with a same size and the self-radiation efficiency of first 20 radiation modes of the 0.40 m $*$ 0.30 m plate is shown in Fig. B2. In low frequencies, lower order radiation modes have a greater impact on sound power. Hence, taking some lower order radiation modes into consider is accurate enough under 1000 Hz. To specify this statement, the SWL comparison between the first 10 radiation modes and LMS results is illustrated in Fig. B3 and the truncation error is of little significance. According to this principle, only the first 5 radiation modes is taken into account for a distinct indication. Given above truncations and dominate modes, the dominant regions in Fig. 12 are decided.

Appendix C: Results of cavity-mode3-714 Hz

As illustrated in Table C1, the absolute value of the mapping coefficient $\{\varphi_3\}^{\mathrm{T}} \boldsymbol{\Theta} \{\phi_i\}$ of 4-ABH-Mode4 is 26.09 and it is smaller than the coefficient of UNI-Mode5 which is 29.14. Meanwhile, for the 4-ABH plate, the cross-cancellation effect still exists, i.e., the modal coordinates are in the same sign for both 4-ABH-Mode4 and 4-ABH-Mode17, but the related coefficients are in the opposite sign.

Therefore, as compared with the UNI plate, smaller SWL and radiation efficiency of the 4-ABH plate are realized at 714 Hz because of the mismatch.

Appendix D: Modal shapes and vibration velocity distributions at 428 Hz

The first 5 radiation modal shapes at 428 Hz are shown in Fig. D2.

Table C1
Modal coordinates and mapping coefficients of plates at 714 Hz.

Structural modes		Modal coordinates (10^{-6})		Mapping coefficients $\{\varphi_2\}^{\mathrm{T}} \boldsymbol{\Theta} \{\phi_i\}$
		Complex form	Absolute value	
Case3	UNI-Mode5	−2.00 + 4.00j	4.47	−29.14
	UNI-Mode10	0.21–0.42j	0.47	14.28
Case6	4-ABH-Mode4	1.00 + 11.00j	11.05	26.09
	4-ABH-Mode17	1.00 + 3.00j	3.16	−28.99
	4-ABH-Mode9	−2.00–2.00j	2.83	4.24

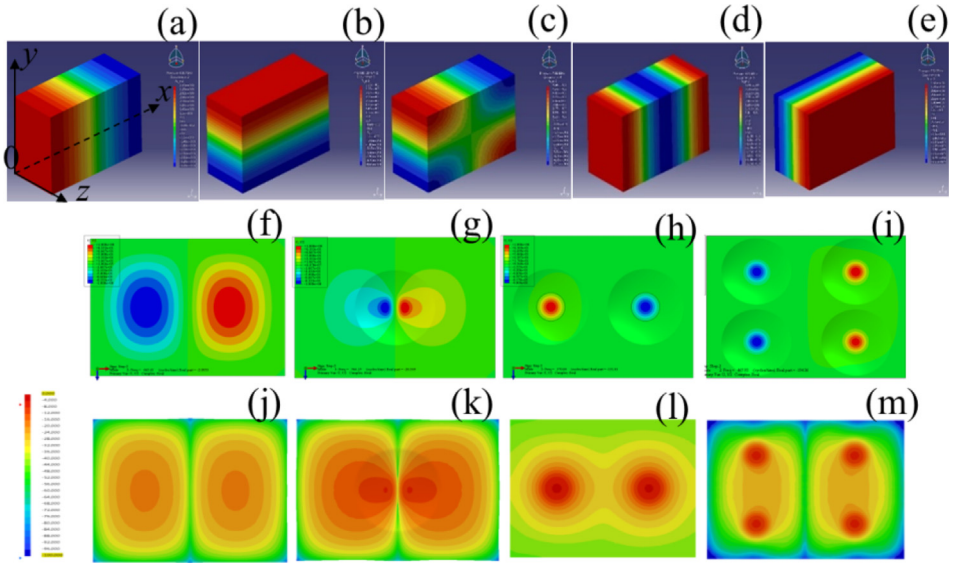

Fig. D1. Modal shapes and vibration velocity distributions. (a)∼(e) cavity modal shapes; (f)∼(i) structural modal shapes; (j)∼(m) vibration velocity distributions at 428 Hz; (a) cavity-mode1-428 Hz; (b) cavity-mode2-571 Hz; (c) cavity-mode3-714 Hz; (d) cavity-mode4-857 Hz; (e) cavity-mode5-952 Hz; (f) UNI-mode2-659 Hz; (g) 1-ABH-mode3-563 Hz; (h) 2-ABH-mode2-368 Hz; (i) 4-ABH-mode2-462 Hz; (j) UNI; (k) 1-ABH; (l) 2-ABH; (m) 4-ABH.

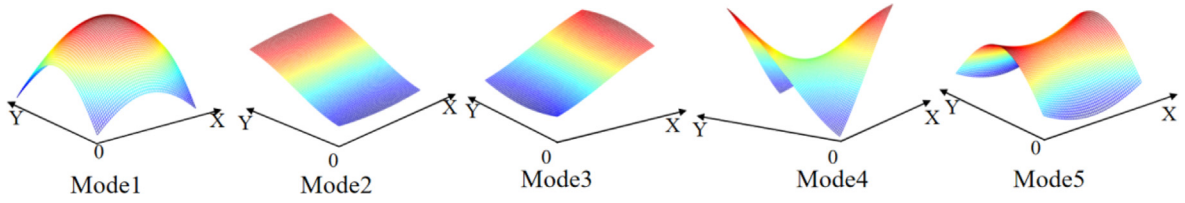

Fig. D2. Radiation Modal shapes at 428 Hz.

References

[1] Cummings A, Chang I-J. Noise breakout from flat-oval ducts. J Sound Vib 1986;106:17–33. https://doi.org/10.1016/S0022-460X(86)80171-7.

[2] Cummings A. Stiffness control of low frequency acoustic transmission through the walls of rectangular ducts. J Sound Vib 1981;74:351–80. https://doi.org/10.1016/0022-460X(81)90304-7.

[3] Astley RJ, Cummings A. A finite element scheme for acoustic transmission through the walls of rectangular ducts: Comparison with experiment. J Sound Vib 1984;92:387–409. https://doi.org/10.1016/0022-460X(84)90387-0.

[4] Lee HP. Natural frequencies and modes of cylindrical polygonal ducts. J Sound Vib 1993;164:182–7. https://doi.org/10.1006/jsvi.1993.1205.

[5] Chang I-J, Cummings A. Higher order mode and multimode acoustic transmission through the walls of flat-oval ducts. J Sound Vib 1986;108:157–64. https://doi.org/10.1016/S0022-460X(86)80319-4.

[6] Cummings A. Higher order mode acoustic transmission through the walls of rectangular ducts. J Sound Vib 1983;90:193–209. https://doi.org/10.1016/0022-460X(83)90528-X.

[7] Jade N, Venkatesham B. Experimental study of breakout noise characteristics of flexible rectangular duct. Mech Syst Signal Process 2018;108:156–72. https://doi.org/10.1016/j.ymssp.2018.02.015.

[8] Venkatesham B, Tiwari M, Munjal ML. Analytical prediction of break-out noise from a reactive rectangular plenum with four flexible walls. J Acoust Soc Am 2010;128:1789–99. https://doi.org/10.1121/1.3463801.

[9] Venkatesham B, Tiwari M, Munjal ML. Analytical prediction of the breakout noise from a rectangular cavity with one compliant wall. J Acoust Soc Am 2008;124:2952–62. https://doi.org/10.1121/1.2977671.

[10] Snyder SD, Hansen CH. Active noise control in ducts: Some physical insights. J Acoust Soc Am 1989;86:184–94. https://doi.org/10.1121/1.398762.

[11] Hansen C, Scott S, Qiu X, Laura B. Active control of noise and vibration. 2nd ed. Boca Raton: CRC Press, Taylor & Francis Group; 2012.

[12] Pelat A, Gautier F, Conlon SC, Semperlotti F. The acoustic black hole: A review of theory and applications. J Sound Vib 2020;476:. https://doi.org/10.1016/j.jsv.2020.115316115316.

[13] Mironov M. Propagation of a flexural wave in a plate whose thickness decreases smoothly to zero in a finite interval. Sov Phys Acoust 1988;34:318–9.

[14] Krylov VV, Winward RETB. Experimental investigation of the acoustic black hole effect for flexural waves in tapered plates. J Sound Vib 2007;300:43–9. https://doi.org/10.1016/j.jsv.2006.07.035.

[15] Krylov VV, Tilman FJBS. Acoustic 'black holes' for flexural waves as effective vibration dampers. J Sound Vib 2004;274:605–19. https://doi.org/10.1016/j.jsv.2003.05.010.

[16] Deng J, Zheng L, Guasch O. Elliptical acoustic black holes for flexural wave lensing in plates. Appl Acoust 2021;174:. https://doi.org/10.1016/j.apacoust.2020.107744107744.

[17] Georgiev VB, Cuenca J, Gautier F, Simon L, Krylov VV. Damping of structural vibrations in beams and elliptical plates using the acoustic black hole effect. J Sound Vib 2011;330:2497–508. https://doi.org/10.1016/j.jsv.2010.12.001.

[18] Tang L, Cheng L, Ji H, Qiu J. Characterization of acoustic black hole effect using a one-dimensional fully-coupled and wavelet-decomposed semi-analytical model. J Sound Vib 2016;374:172–84. https://doi.org/10.1016/j.jsv.2016.03.031.

[19] Deng J, Guasch O, Zheng L. Ring-shaped acoustic black holes for broadband vibration isolation in plates. J Sound Vib 2019;458:109–22. https://doi.org/10.1016/j.jsv.2019.06.017.

[20] Deng J, Guasch O, Zheng L, Song T, Cao Y. Semi-analytical model of an acoustic black hole piezoelectric bimorph cantilever for energy harvesting. J Sound Vib 2021;494:. https://doi.org/10.1016/j.jsv.2020.115790115790.

[21] Zhou T, Tang L, Ji H, Qiu J, Cheng L. Dynamic and static properties of double-layered compound acoustic black hole structures. Int J Appl Mech 2017;09:1750074. https://doi.org/10.1142/S1758825117500740.

[22] Tang L, Cheng L. Impaired sound radiation in plates with periodic tunneled Acoustic Black Holes. Mech Syst Signal Process 2020;135:. https://doi.org/10.1016/j.ymssp.2019.106410106410.

[23] Wang X, Ji H, Qiu J, Cheng L. Wavenumber domain analyses of vibro-acoustic decoupling and noise attenuation in a plate-cavity system enclosed by an acoustic black hole plate. J Acoust Soc Am 2019;146:72–84. https://doi.org/10.1121/1.5114821.

[24] Liang X, Chu J, Tan J, Nie S, Liu B, Zheng X, et al. Spontaneous catastrophe behaviour in acoustic black holes at low frequencies. Appl Acoust 2021;180:. https://doi.org/10.1016/j.apacoust.2021.108109108109.

[25] Gao N, Wei Z, Zhang R, Hou H. Low-frequency elastic wave attenuation in a composite acoustic black hole beam. Appl Acoust 2019;154:68–76. https://doi.org/10.1016/j.apacoust.2019.04.029.

[26] Gao N, Guo X, Deng J, Cheng B, Hou H. Elastic wave modulation of double-leaf ABH beam embedded mass oscillator. Appl Acoust 2021;173:. https://doi.org/10.1016/j.apacoust.2020.107694107694.
[27] Lee JY, Jeon W. Vibration damping using a spiral acoustic black holea). J Acoust Soc Am 2017;141:1437–45. https://doi.org/10.1121/1.4976687.
[28] Park S, Kim M, Jeon W. Experimental validation of vibration damping using an Archimedean spiral acoustic black hole. J Sound Vib 2019;459:. https://doi.org/10.1016/j.jsv.2019.07.004114838.
[29] Ji H, Wang N, Zhang C, Wang X, Cheng L, Qiu J. A vibration absorber based on two-dimensional acoustic black holes. J Sound Vib 2021;500:. https://doi.org/10.1016/j.jsv.2021.116024116024.
[30] Ji H, Zhao X, Wang N, Huang W, Qiu J, Cheng L. A circular eccentric vibration absorber with circumferentially graded acoustic black hole features. J Vib Acoust 2022;144:. https://doi.org/10.1115/1.4053475021014.
[31] Ma L, Cheng L. Sound radiation and transonic boundaries of a plate with an acoustic black hole. J Acoust Soc Am 2019;145:164–72. https://doi.org/10.1121/1.5081680.
[32] Ma L, Cheng L. Numerical and experimental benchmark solutions on vibration and sound radiation of an Acoustic Black Hole plate. Appl Acoust 2020;163:. https://doi.org/10.1016/j.apacoust.2020.107223107223.
[33] Deng J, Guasch O, Maxit L, Zheng L. Annular acoustic black holes to reduce sound radiation from cylindrical shells. Mech Syst Signal Process 2021;158:. https://doi.org/10.1016/j.ymssp.2021.107722107722.
[34] Tang L, Gao N, Xu J, Chen K, Cheng L. A light-weight periodic plate with embedded acoustic black holes and bandgaps for broadband sound radiation reduction. J Acoust Soc Am 2021;150:3532–43. https://doi.org/10.1121/10.0007067.
[35] Feurtado PA, Conlon SC. Wavenumber transform analysis for acoustic black hole design. J Acoust Soc Am 2016;140:718–27. https://doi.org/10.1121/1.4959023.
[36] Deng J, Zheng L. Noise reduction via three types of acoustic black holes. Mech Syst Signal Process 2022;165:. https://doi.org/10.1016/j.ymssp.2021.108323108323.
[37] Deng J, Gao N, Chen X, Pu H, Guo J. Underwater sound radiation from a Mindlin plate with an acoustic black hole. Ocean Eng 2023;278:. https://doi.org/10.1016/j.oceaneng.2023.114376114376.
[38] Ji H, Wang X, Qiu J, Cheng L, Wu Y, Zhang C. Noise reduction inside a cavity coupled to a flexible plate with embedded 2-D acoustic black holes. J Sound Vib 2019;455:324–38. https://doi.org/10.1016/j.jsv.2019.05.004.
[39] Xiong Y, Smith EC, Conlon SC. Transmission loss of plates with embedded multi-scale and tuned acoustic black holes. J Acoust Soc Am 2021;150:2282–93. https://doi.org/10.1121/10.0006442.
[40] Du X, Huang D, Fu Q, Zhang J. Effects of acoustic black hole parameters and damping layer on sound insulation performance of ABH circular plate. Appl Sci 2019;9:5366. https://doi.org/10.3390/app9245366.
[41] Deng J, Guasch O, Maxit L, Zheng L. Transmission loss of plates with multiple embedded acoustic black holes using statistical modal energy distribution analysis. Mech Syst Signal Process 2021;150:. https://doi.org/10.1016/j.ymssp.2020.107262107262.
[42] Fahy F, Gardonio P. Sound and structural vibration: radiation, transmission and response. Noise Control Eng J 2007;55(3):373.
[43] Jacobsen F, Juhl PM. Fundamentals of General Linear Acoustics. Chichester, West Sussex, United Kingdom: John Wiley & Sons Inc; 2013.
[44] Elliott SJ, Johnson ME. Radiation modes and the active control of sound power. J Acoust Soc Am 1993;94:2194–204. https://doi.org/10.1121/1.407490.
[45] Currey MN, Cunefare KA. The radiation modes of baffled finite plates. J Acoust Soc Am 1995;98:1570–80. https://doi.org/10.1121/1.413423.
[46] Bies DA, Hansen CH, Howard CQ. Engineering noise control, Fifth edition, CRC Press. Boca Raton: Taylor & Francis Group; 2018.
[47] Deng J, Guasch O, Maxit L, Gao N. Sound radiation and non-negative intensity of a metaplate consisting of an acoustic black hole plus local resonators. Compos Struct 2023;304:. https://doi.org/10.1016/j.compstruct.2022.116423116423.
[48] Conlon SC, Fahnline JB, Semperlotti F. Numerical analysis of the vibroacoustic properties of plates with embedded grids of acoustic black holes. J Acoust Soc Am 2015;137:447–57. https://doi.org/10.1121/1.4904501.